

Time-delay interferometry noise transfer functions for LISA

Dam Quang Nam,¹ Yves Lemière,² Antoine Petiteau,^{3,1} Jean-Baptiste Bayle,⁴ Olaf Hartwig,⁵ Joseph Martino,¹ and Martin Staab^{6,7}

¹*Université Paris Cité, CNRS, Astroparticule et Cosmologie, F-75013 Paris, France*

²*Normandie Univ, ENSICAEN, UNICAEN, CNRS/IN2P3, LPC Caen, 14000 Caen, France*

³*IRFU, CEA, Université Paris-Saclay, F-91191, Gif-sur-Yvette, France*

⁴*University of Glasgow, Glasgow G12 8QQ, United Kingdom*

⁵*SYRTE, Observatoire de Paris, Université PSL, CNRS,*

Sorbonne Université, LNE, 61 avenue de l'Observatoire, 75014 Paris, France

⁶*Max Planck Institute for Gravitational Physics (Albert Einstein Institute), D-30167 Hannover, Germany*

⁷*Leibniz Universität Hannover, D-30167 Hannover, Germany*

The Laser Interferometry Space Antenna (LISA) mission is the future space-based gravitational-wave (GW) observatory of the European Space Agency. It is formed by three spacecraft exchanging laser beams in order to form multiple interferometers. The data streams to be used in order to extract the large number and variety of GW sources are time-delay interferometry (TDI) data. One important processing step to produce these data is the TDI on-ground processing, which recombines multiple interferometric on-board measurements to remove certain noise sources from the data, such as laser frequency noise or spacecraft jitter noise. The LISA noise budget is therefore expressed at the TDI level in order to account for the different TDI transfer functions applied for each noise source and thus estimate their real weight on mission performance. In this study, we present an update model for the beams, measurements and TDI, with several approximations to derive the noise transfer functions. The laser locking and noise correlation are taken into account to see their impact in the transfer functions. A methodology for such a derivation has been established in detail, as well as verification procedures against simulated data. It results in a set of transfer functions, which are now used by the LISA project, in particular in its performance model. Using these transfer functions, realistic noise curves for various instrumental configurations are provided to data analysis algorithms and used for instrument design.

I. INTRODUCTION

The Laser Interferometer Space Antenna (LISA) [1, 2] is a space-based gravitational wave observatory that aims to measure gravitational waves (GWs) in the millihertz range. The mission is led by European Space Agency (ESA), with National Aeronautic and Space Administration (NASA) as a junior partner, and European member states contributing to both hardware and processing. LISA will enable the observation of parts of the Universe invisible by other means, such as black holes and binaries of compact objects. Furthermore, we will be able to study the very early Universe soon after the big bang, and possibly discover yet completely unknown objects. LISA will enhance our knowledge about astrophysics, cosmology and fundamental physics.

LISA is composed of three spacecraft (S/C) in heliocentric orbits, forming an equilateral triangle constellation. The constellation trajectory is in the ecliptic plane at one astronomical unit from the Sun, and leading or trailing Earth on its orbit, with an angular separation of 10 to 30 degrees. This distance from Earth is chosen to minimize *arm-breathing* induced by the Earth while still being close enough to allow communications.

The S/C exchange laser beams to form multiple interferometers. By monitoring the changes in distance between free-falling test-masses inside the spacecraft, LISA senses gravitational waves. Six laser beams, imprinted by the gravitational waves, connecting the local and distant

test-masses, interfere with local laser beams and permit measurements with picometer precision. Achieving this precision requires the suppression of many technical noise sources, the largest of which is laser frequency noise. It is expected to be several orders of magnitude above gravitational wave (GW) signals. Time delay interferometry (TDI) [3–10] will suppress this dominant source of noise by 8 orders of magnitude, bringing it below secondary noises and GW signals. The basic idea of TDI is to combine time-shifted phase or frequency measurements from the three satellites on-ground to synthesize virtual interferometers which are naturally insensitive to laser frequency noise, but still sensitive to GW signals. Other noise sources that are above the requirements [2], need to be suppressed as part of the TDI algorithm, such as clock noise. Additional algorithms are developed to suppress these noise sources and then integrated to the latest version of the TDI algorithm [11].

To define the instrument performances, two classes of noises are considered: suppressed noises and unsuppressed noises. The suppressed noises are dominant in LISA measurements and should be mitigated by some on-board or offline data processing (e.g., TDI), such as laser frequency noise [12, 13], spacecraft jitter noise, clock and ranging noises [11], tilt-to-length [14]. The unsuppressed ones are secondary noises, such as test-mass acceleration noise, optical path noises, readout noises, backlink, etc. However, they will constitute the dominant contribution to the LISA instrument noise budget after mitigation of all suppressed noises. This article will present the an-

analytical formulation of how unsuppressed noises propagate through TDI and the validation of these formulations. The analytical transfer functions are expressed in TDI second generation, which is required for laser frequency noise suppression in realistic orbits with varying armlengths [3].

The transfer functions of second generation TDI for the suppressed noises (laser frequency noise [12, 13], clock jitter noise [11, 15] and for the secondary noises [16] have already investigated with ideal conditions, i.e., equal armlengths and same statistical property of the same type noises in different movable optical subassemblies (MOSAs). In this article, we work out the transfer functions of unsuppressed noises without these assumptions. In addition, the impact of laser locking and noise correlation in the transfer function is also investigated. In fact, laser locking and frequency plan were taken into account in some studies of the laser frequency noise reduction, see e.g., [17, 18], but not for the secondary noises. Therefore, we can extend the understanding of the propagation of unsuppressed noise in realistic configuration, which could change the LISA noise budget.

The article is structured as follows. In Sec. II, we introduce the LISA convention, unsuppressed noises, its beam model and measurements, and TDI formulation. The laser locking and some correlation scenarios are also addressed in this section. Then, Sec. III will focus on the methodology to get the power spectral density of the signal as a function of frequency. Some examples show the detailed computation for analytical noise transfer functions with different configurations. At the end of Sec. III, we present the procedure to compare an approximated formulation with instrument simulations performed with LISANode. Section IV will be dedicated to the summary of analytical noise transfer functions and the simulation validation. Finally, we conclude in Sec. V.

II. LISA MODEL

A. Convention

In this article, we follow the convention for the LISA constellation proposed by LISA Consortium ([19]). The indexing is summarized on Fig. 1. Spacecraft are indexed 1, 2, 3 clockwise when looking down at their solar panels. Each of them hosts two MOSAs which include the test-mass and its housing, the optical bench and the telescope. A laser source is associated with each movable optical subassembly (MOSA). MOSAs on each spacecraft are indexed with two numbers ij :

- The first number i is the index of the S/C the MOSA is mounted on, i.e., the local S/C.
- The second number j is the index of the S/C the MOSA points to.

All subsystems of the MOSA, the associated laser and the optical measurements are indexed according to this

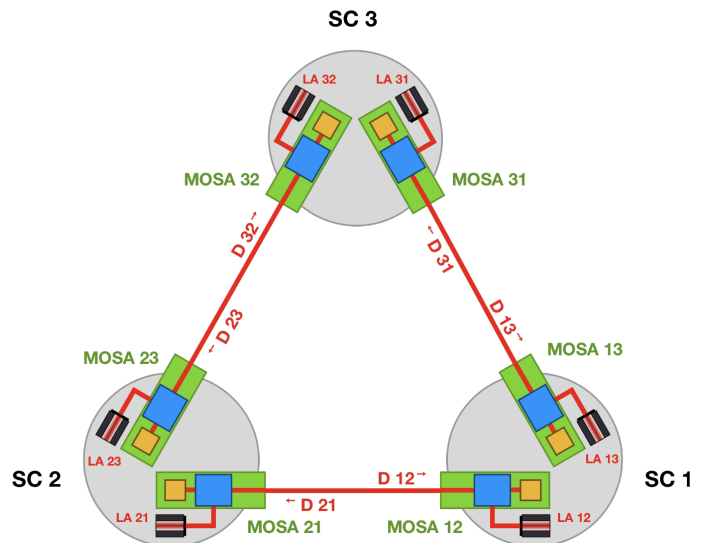


FIG. 1. LISA constellation convention. The MOSA hosted on spacecraft 1 (SC 1) pointing at spacecraft 2 (SC 2) is labeled MOSA_{12} . Each element hosted on this MOSA and the associated laser source will share the same indexes. For example the noise due to the laser associated to the MOSA_{12} will be labeled p_{12} .

MOSA. There are three main interferometric measurements in each MOSA: inter-satellite interferometer (ISI), test-mass interferometer (TMI) and reference interferometer (RFI), which are respectively denoted as isi , tmi , rfi .¹ The ISI measurement is monitoring the distance between two optical benches (OBs) in difference spacecraft, while the TMI measures the distance between the test-mass (TM) and OB in the same MOSA. The RFI measurement is used to mitigate the spacecraft jitter noise (relation motion between test-mass and optical bench attached in spacecraft), and to reduce the number of free-running laser as we see later in Sec. II G. The detailed formulation of these measurements will be presented in Secs. II C and II D.

We define $L_{ij}(t)$ as the light travel time from S/C j to S/C i , in seconds. For the propagation of light, we denote the propagation delay operator² by \mathbf{D}_{ij} , so that $\mathbf{D}_{ij}u(t) = u(t - L_{ij}(t))$ for any time series $u(t)$. We also use the TDI delay operator \mathcal{D}_{ij} , such that $\mathcal{D}_{ij}u(t) = x(t - \hat{L}_{ij}(t))$, where $\hat{L}_{ij}(t)$ is the estimate of the light travel time $L_{ij}(t)$. For nested delay operators, we use the short hand notation $d_{i_1 i_2 \dots i_n} \equiv d_{i_1 i_2} d_{i_2 i_3} \dots d_{i_{n-1} i_n}$, where d could be \mathbf{D} or \mathcal{D} . In general, those delay operators are not commutative since light travel times evolve with time. If we use the commutator notation of $[A, B] = AB - BA$

¹ To feed the clock noise reduction algorithm, we also need the sideband measurements in the isi and the rfi [11].

² Technically, since the measurements will be expressed in relative frequency fluctuation units, \mathbf{D}_{ij} is a Doppler-delay operator $\mathbf{D}_{ij}u(t) = (1 - \dot{L}_{ij}(t))u(t - L_{ij}(t))$ (see Sec. 7.2 of [10]).

then $[\mathbf{D}_{ij}, \mathbf{D}_{mn}]u(t) \neq 0$ when $(i, j) \neq (m, n)$. But if delay times or armlengths are assumed to be constant, delay operators become commutative. We will use this to simplify the computation process.

Another process we indicate using an operator is the action of the antialiasing filters, which are used to prevent power folding in the band of interest during decimation. Its operator is denoted as \mathcal{F} , such as $\mathcal{F}u(t) = (f * u)(t)$, where the asterisk stands for the convolution of time series $u(t)$ with the filter kernel $f(t)$.

The GW signal measured in ISI_{ij} , caused by the accumulated delay of the beam received on S/C i from S/C j due to a GW, is labeled H_{ij} .

The wavelength of laser associated to MOSA_{ij} is λ_{ij} and its frequency is denoted as $\nu_{ij} = c/\lambda_{ij}$. We also define the frequency of the laser beam received by MOSA_{ij} from MOSA_{ji} as $\nu_{i \leftarrow j}$. Due to the Doppler shift along the link L_{ji} , $\nu_{i \leftarrow j} \neq \nu_{ji}$. The laser frequency ν is the sum of nominal frequency (carrier or sideband — THz), an offset frequency (Doppler and laser locking — MHz) and small fluctuations (noises and GWs — nHz to Hz). The interferometric signals in LISA are the heterodyne beatnote frequencies, i.e., the frequency differences between the frequencies of associated beams (offsets and small fluctuations). Their signs are (beatnote polarities) θ^{isi} and θ^{rfi} for ISI and TMI/RFI signals, respectively.

$$\begin{cases} \theta_{ij}^{\text{isi}} &= \text{sign}(\omega_{i \leftarrow j} - \omega_{ij}), \\ \theta_{ij}^{\text{tmi}} = \theta_{ij}^{\text{rfi}} &= \text{sign}(\omega_{ik} - \omega_{ij}), \end{cases} \quad (1)$$

where $\omega = 2\pi\nu$, (i, j, k) matches every cyclic permutation of $(1, 2, 3)$. In general, $\theta_{ij}^{\text{isi}} \neq -\theta_{ji}^{\text{isi}}$ but $\theta_{ij}^{\text{rfi}} = -\theta_{ik}^{\text{rfi}}$.

B. List of unsuppressed noises

The laser frequency noise is the dominant noise source in LISA, and reduced by TDI postprocessing algorithm (see Sec. IIG). Other noises that are not suppressed by TDI or other postprocessing algorithms are called unsuppressed noises. Unsuppressed noises are subdominant (for example with respect to laser frequency noise or clock noise) but once these dominant noises have been suppressed, they contribute to the LISA noise budget. It is therefore necessary to study their propagation through TDI.

The measurements will be either in phase or frequency, or a mixture of both. The final choice is not yet made. Since the noises we are interested are expressed as small fluctuations (phase or frequency), we will assume that the measurements are in relative frequency fluctuations. It is also the unit used for most of the GW analyses.

We will denote the LISA instrumental noises as follows:

- p_{ij} : laser frequency noise (free-running or locked, see Sec. IIF) of the laser on MOSA_{ij} ;
- $\delta_{ij} = \vec{\delta}_{ij} \cdot \hat{\mathbf{n}}_{ji}/c$: projection of test-mass ij jitter noise vector $\vec{\delta}_{ij}$ onto the sensitive axis. $\hat{\mathbf{n}}_{ji}$ is the

reference axis for the MOSA_{ij} , i.e., from test-mass to optical bench (OB) (see Figs 1 and 2). We assume that all measurements are in fractional frequency units. The test-mass jitter noise is expressed in velocity (m/s), so we need the factor $1/c$ (see [8] for the detailed derivation);

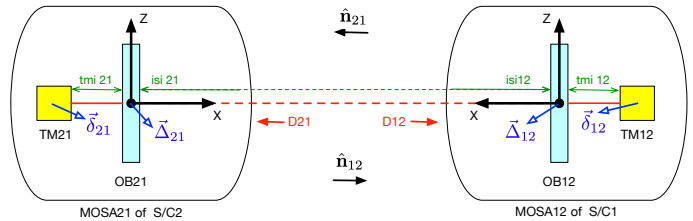


FIG. 2. Conventions for direction of beams and motions for MOSA_{12} and MOSA_{21} . The reference X axis for MOSA_{12} is equal to $\hat{\mathbf{n}}_{21}$.

- $\Delta_{ij} = \vec{\Delta}_{ij} \cdot \hat{\mathbf{n}}_{ji}/c$: projection of MOSA_{ij} jitter noise vector $\vec{\Delta}_{ij}$ onto the sensitive axis (longitudinal axis);
- $\mu_{ij \rightarrow ik}^x$: backlink noise for the x measurement, $x \in \{\text{tmi}, \text{rfi}\}$. This noise is dominated by straylight in the optical fiber connecting two MOSAs of the same S/C [from OB_{ij} to OB_{ik} , where (i, j, k) is the set of combination of $(1, 2, 3)$]. In general, this noise is nonreciprocal, i.e., $\mu_{ik \rightarrow ij}^x \neq \mu_{ij \rightarrow ik}^x$.
- $N_{x,ij}^{ro}$: readout noise for the x measurement of OB_{ij} , $x \in \{\text{isi}, \text{tmi}, \text{rfi}\}$;
- $N_{\alpha,ij}^{\text{op}}$: generic optical path (OP) noise term due to optical path fluctuations on OB_{ij} . α refers to:
 - TX/isi : OP noise on the beam transmitted to the distant S/C induced by the sending S/C;
 - RX/isi : OP noise on the beam received from the distant S/C induced by the receiving S/C;
 - tmi : OP noise on adjacent beam in the TMI measurement;
 - rfi : OP noise on adjacent beam in the RFI measurement;
 - loc/isi : OP noise on local beam in the ISI measurement;
 - loc/tmi : OP noise on local beam in the TMI measurement;
 - loc/rfi : OP noise on local beam in the RFI measurement.

C. Beam modeling

In order to model the interferometric measurement, we start by modeling the beams that interfere in terms of

combination of noises. The main six beams of the three interferometers in the MOSA 12 are described as

$$b_{\text{isi},21 \rightarrow 12} = \mathbf{D}_{12} \left[p_{21} + N_{TX/\text{isi},21}^{\text{op}} - \frac{1}{c} \hat{\mathbf{n}}_{12} \cdot \vec{\Delta}_{21} \right] + H_{12} - \frac{1}{c} \hat{\mathbf{n}}_{21} \cdot \vec{\Delta}_{12} + N_{RX/\text{isi},12}^{\text{op}} \quad (2a)$$

$$b_{\text{tmi},13 \rightarrow 12} = p_{13} + \mu_{13 \rightarrow 12}^{\text{tmi}} + N_{\text{tmi},12}^{\text{op}} \quad (2b)$$

$$b_{\text{rfi},13 \rightarrow 12} = p_{13} + \mu_{13 \rightarrow 12}^{\text{rfi}} + N_{\text{rfi},12}^{\text{op}} \quad (2c)$$

$$b_{\text{isi},12 \rightarrow 12} = p_{12} + N_{\text{loc}/\text{isi},12}^{\text{op}} \quad (2d)$$

$$b_{\text{tmi},12 \rightarrow 12} = p_{12} + \frac{2}{c} \hat{\mathbf{n}}_{21} \cdot (\vec{\Delta}_{12} - \vec{\delta}_{12}) + N_{\text{loc}/\text{tmi},12}^{\text{op}} \quad (2e)$$

$$b_{\text{rfi},12 \rightarrow 12} = p_{12} + N_{\text{loc}/\text{rfi},12}^{\text{op}} \quad (2f)$$

where

- $b_{\text{isi},21 \rightarrow 12}$ is the beam from MOSA 21 received by MOSA 12,
- $b_{\text{rfi},13 \rightarrow 12}$ and $b_{\text{tmi},13 \rightarrow 12}$ are the beams propagating from MOSA 13 to MOSA 12 through the backlink, which respectively contribute to RFI and TMI measurements.
- $b_{x,12 \rightarrow 12}$ are the local beams of the MOSA 12 with $x \in \{\text{isi}, \text{tmi}, \text{rfi}\}$.

In the current design, the local beam of the TMI, $b_{\text{tmi},12 \rightarrow 12}$, is bouncing on the test-mass. The sign convention is such that if the test-mass moves toward the OB, i.e., $\vec{\delta}_{12}$ points in the positive direction (X axis of MOSA 21, $\hat{\mathbf{n}}_{21}$, see Fig. 2), the optical path on the beam $b_{\text{tmi},12 \rightarrow 12}$ decreases. If the OB moves away from the test-mass, i.e., $\vec{\Delta}_{12}$ points in the positive direction, the optical path on the beam $b_{\text{tmi},12 \rightarrow 12}$ increases while it decreases on $b_{\text{isi},21 \rightarrow 12}$.

The beams in MOSA 13 are constructed in the same way. One can easily write them from the formulas of MOSA 12 by replacing index 2 by 3 everywhere. The beams in the other MOSAs can be deduced by circular permutation of indices (1 \rightarrow 2 \rightarrow 3 \rightarrow 1).

D. Interferometer measurement

Using those beams, we can construct the three main interferometric measurements, for example in the MOSA 12, as follows

$$\begin{cases} \text{isi}_{12} &= \mathcal{F} \left[\theta_{12}^{\text{isi}} (b_{\text{isi},21 \rightarrow 12} - b_{\text{isi},12 \rightarrow 12}) + N_{\text{isi},12}^{ro} \right] \\ \text{tmi}_{12} &= \mathcal{F} \left[\theta_{12}^{\text{tmi}} (b_{\text{tmi},13 \rightarrow 12} - b_{\text{tmi},12 \rightarrow 12}) + N_{\text{tmi},12}^{ro} \right] \\ \text{rfi}_{12} &= \mathcal{F} \left[\theta_{12}^{\text{rfi}} (b_{\text{rfi},13 \rightarrow 12} - b_{\text{rfi},12 \rightarrow 12}) + N_{\text{rfi},12}^{ro} \right]. \end{cases} \quad (3)$$

As indicated before, we are interested in the small fluctuations from noises and GWs, and so neglect the beat-note offsets in the interferometric measurements³. All measurements are expressed in relative frequency fluctuation units. In phase units, these equations are similar, with additional conversion factors.

E. Correlations

Even though, the impact of correlations has been discussed in early TDI studies [20]. In most studies, as for example [1, 2, 21, 22], the LISA Instrument noise performance are assessed as uncorrelated single link contribution from optical measurement system and test-mass acceleration. This assumption simplifies the calculation of noise propagation but may induce non-negligible errors in the estimation of LISA performances. To quantitatively estimate the deviation from the ideal case, we will consider some generic scenarios of correlation in this study. Furthermore, we can split the noises into two parts, the correlated and uncorrelated terms, and derive their transfer functions separately.

One obvious correlation scenario is related to the thermo-mechanical optical path noises in the telescope⁴. Since the same telescope is used for both sending and receiving beams, it will imprint an identical noise at the ISI beam, located at both end of a link. The optical path noise on the emitted beam $N_{TX/\text{isi},ij}^{\text{op}}$ and the received beam $N_{RX/\text{isi},ij}^{\text{op}}$ in the telescope of MOSA ij are fully correlated:

$$N_{TX/\text{isi},ij}^{\text{op}} = N_{RX/\text{isi},ij}^{\text{op}} \quad (4)$$

Another possible correlation scenario is related to test-mass acceleration noise. The two test-masses share the same S/C and thus will likely have correlated source of noises like temperature driven noises (stiffness, symmetric outgassing), cross-talk of S/C jitter, coupling with local and interplanetary magnetic fields or local gravity field fluctuation. We express it by the following correlation relation

$$\vec{\delta}_{ij} \cdot \hat{\mathbf{n}}_j = \gamma \vec{\delta}_{ik} \cdot \hat{\mathbf{n}}_{ki}, \quad (5)$$

where γ is the correlation factor and (i, j, k) can be any permutation of (1, 2, 3). γ is 1 in the case of fully correlated noise, or -1 in case of anticorrelation. We will

³ The beatnote polarities $\theta^{\text{isi}}, \theta^{\text{rfi}}$ depend on the total laser frequencies of the interfering beams. However, they only define the signs of the beatnote measurements.

⁴ While the optical path noise enters in the ISI measurements in the same way as the MOSA jitter noise, it is not canceled by the time-delay interferometry algorithm, as described later in Sec. II G, because it does not appear in the TMI measurements.

derive the propagation of the fully correlated acceleration noise in Sec. IV. The transfer functions for fully correlated and anticorrelated acceleration noise, fully correlated and anticorrelated adjacent (same S/C) interferometer noise and fully correlated optical path noise at the same telescope are also given (see Tables II and III).

F. Frequency planning — Laser locking scheme

The intersatellite separation distance varies in time due to orbital dynamics. As a consequence, the laser beam coming from the distant S/C is frequency-shifted by about 10 MHz according to the Doppler effect. The laser frequencies used for the interferometric measurement are slightly offset. There is a time evolution of the beatnote between the two beams used to measure phase shift via heterodyne interferometry.

The optical measurement system tracks the beatnote frequencies in the range of 5 to 25 MHz, which is not compatible with free running lasers and Doppler-shifted beams. To accommodate this constraint, we lock the lasers by controlling the frequency of a laser (therefore the beatnote frequencies) such that they remain equal to a pre-programmed reference value [23]. We use the RFI measurement to phase-lock a laser with its adjacent laser in the same S/C (local locking), and the ISI signal to lock the local laser to the distant laser (distant locking). In the end, 5 of 6 lasers will be locked on the primary laser. In this study, we assume that laser frequency control works perfectly so the locking beatnote offset, laser frequency offset plus the Doppler shift if it is distant locking, is exactly equal to the desired value. We also do not consider the beatnote offset in the interferometric measurement, as discussed in Sec. IID. The constraint equation of the beatnote fluctuation is used without filter since the laser locking control loop operates at high frequency before measurements are filtered and downsampled [10].

In this study, the configuration N4-32 (cfg_N2c in [23]) has been used⁵. The detailed phase-locking is shown on Fig. 3. The constraints on the beatnote fluctuations are

$$\text{isi}_{21}^{\times} = 0, \quad (6a)$$

$$\text{rfi}_{31}^{\times} = 0, \quad (6b)$$

$$\text{isi}_{13}^{\times} = 0, \quad (6c)$$

$$\text{rfi}_{12}^{\times} = 0, \quad (6d)$$

$$\text{isi}_{23}^{\times} = 0, \quad (6e)$$

where \times indicates the unfiltered and nondownsamped signal. These equations yield the following formulation for the five locked laser frequency fluctuations:

$$p_{23} = \theta_{23}^{\text{isi}} N_{\text{isi},23}^{\text{ro}} + b_{\text{isi},32 \rightarrow 23} - N_{\text{loc}/\text{isi},23}^{\text{op}}, \quad (7a)$$

$$p_{31} = \theta_{31}^{\text{rfi}} N_{\text{rfi},31}^{\text{ro}} + b_{\text{rfi},32 \rightarrow 31} - N_{\text{loc}/\text{rfi},31}^{\text{op}}, \quad (7b)$$

$$p_{13} = \theta_{13}^{\text{isi}} N_{\text{isi},13}^{\text{ro}} + b_{\text{isi},31 \rightarrow 13} - N_{\text{loc}/\text{isi},13}^{\text{op}}, \quad (7c)$$

$$p_{12} = \theta_{12}^{\text{rfi}} N_{\text{rfi},12}^{\text{ro}} + b_{\text{rfi},13 \rightarrow 12} - N_{\text{loc}/\text{rfi},12}^{\text{op}}, \quad (7d)$$

$$p_{21} = \theta_{21}^{\text{isi}} N_{\text{isi},21}^{\text{ro}} + b_{\text{isi},12 \rightarrow 21} - N_{\text{loc}/\text{isi},21}^{\text{op}}. \quad (7e)$$

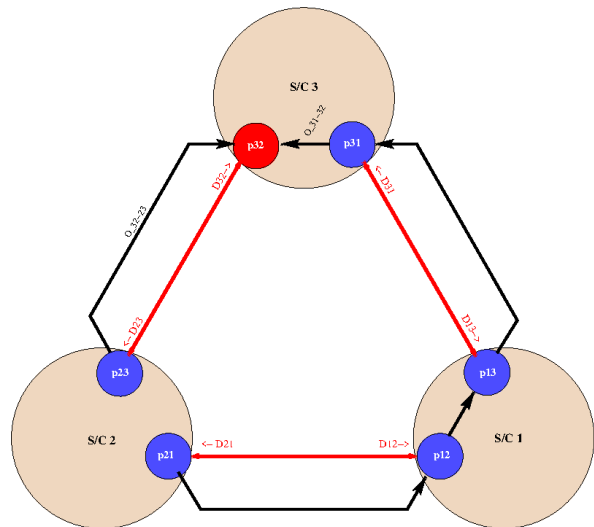


FIG. 3. Frequency planning configuration N4-32 (cfg_N2c in [23]). The primary laser is 32 with frequency fluctuations p_{32} . The other lasers are locked via RFI measurements (31 and 12) or via ISI measurements (13, 21 and 23).

G. Time-delay interferometry formulation

Due to the unequal armlengths entering the ISI measurements, laser noise cannot be canceled out when two beams interfere at the photodiode. While the lasers are prestabilized, the laser frequency noise is still too high and will be a few orders of magnitude above the mission requirements [24]. The postprocessing algorithm called TDI will reduce the laser frequency noise below the requirements by building an equal-arm interferometer (combining time-shifted raw phase measurements). It has been showed that TDI preserves the gravitational wave signal [5, 25, 26].

The TDI formulation involves several steps, which yield the TDI variables. The first step is to suppress the spacecraft motion (also dubbed optical bench displacement) noise Δ_{ij} , by introducing the intermediary variables ξ_{ij} . The idea is to extract the spacecraft jitter noise from the test-mass interferometer (TMI) measurement by subtracting it with reference (RFI) one, so that the laser frequency noise both contained in TMI and RFI

⁵ We used N4-32 because it was the preferred configuration when this study started. Currently the preferred configuration is N1-12 but this does not change the final results which are independent of the locking configuration.

are canceled out as the result. Then we subtract that result by the ISI measurement, which also contains the same noise term, to annihilate the spacecraft jitter noise.

$$\xi_{12} = \text{isi}_{12} - \theta_{12}^{\text{isi}} \theta_{12}^{\text{rfi}} \frac{\lambda_{12}}{\lambda_{21}} \frac{\text{tmi}_{12}(t) - \text{rfi}_{12}(t)}{2} - \theta_{12}^{\text{isi}} \theta_{21}^{\text{rfi}} \frac{\mathcal{D}_{12} [\text{tmi}_{21}(t) - \text{rfi}_{21}(t)]}{2}, \quad (8)$$

$$\xi_{13} = \text{isi}_{13} - \theta_{13}^{\text{isi}} \theta_{13}^{\text{rfi}} \frac{\lambda_{13}}{\lambda_{31}} \frac{\text{tmi}_{13}(t) - \text{rfi}_{13}(t)}{2} - \theta_{13}^{\text{isi}} \theta_{31}^{\text{rfi}} \frac{\mathcal{D}_{13} [\text{tmi}_{31}(t) - \text{rfi}_{31}(t)]}{2}. \quad (9)$$

Then, we can build the second intermediary variables to reduce the number of laser noises by half using the RFI measurements.

$$\eta_{12}(t) = \theta_{12}^{\text{isi}} \xi_{12}(t) + \frac{\mathcal{D}_{12} [\theta_{21}^{\text{rfi}} \text{rfi}_{21}(t) - \theta_{23}^{\text{rfi}} \text{rfi}_{23}(t)]}{2}, \quad (10)$$

$$\eta_{13}(t) = \theta_{13}^{\text{isi}} \xi_{13}(t) - \frac{\theta_{13}^{\text{rfi}} \text{rfi}_{13}(t) - \theta_{12}^{\text{rfi}} \text{rfi}_{12}(t)}{2}. \quad (11)$$

From the intermediary variables η_{ij} , we can build the TDI variables that reduce laser noise. Several TDI combinations exist [5, 9, 10, 27]. In this article, we focus on the second generation Michelson variables X_2, Y_2, Z_2 , where each of the two virtual beams of the TDI Michelson [5], visits both distant spacecraft twice. We compute X_2 as

$$X_2 = (1 - \mathcal{D}_{12131}) [(\eta_{13} + \mathcal{D}_{13}\eta_{31}) + \mathcal{D}_{131} (\eta_{12} + \mathcal{D}_{12}\eta_{21})] - (1 - \mathcal{D}_{13121}) [(\eta_{12} + \mathcal{D}_{12}\eta_{21}) + \mathcal{D}_{121} (\eta_{13} + \mathcal{D}_{13}\eta_{31})].$$

The other two Michelson combinations Y_2 and Z_2 are derived from this equation by circularly permuting all indices.

III. METHODOLOGY

In this section, we introduce our method to compute the TDI transfer function of the noise propagation, using as an example test-mass acceleration noise. Approximations for the simplified result are then justified. Finally, we validate the analytic transfer functions of several noises using the LISANode simulator.

A. PSD/CSD computation

We will briefly introduce a method for calculating the spectral density, which follows the procedure used in the software [28]. The cross power spectral density (CSD) of two signals $u(t)$ and $v(t)$ can be defined as

$$S_{uv}(f) = \text{CSD}[u, v] = \lim_{T \rightarrow \infty} \frac{1}{T} \tilde{u}_T^*(f) \tilde{v}_T(f) \equiv \langle \tilde{u}^*(f) \tilde{v}(f) \rangle. \quad (13)$$

where $\tilde{u}(f)$ is the Fourier transform of $u(t)$ at the frequency f , a^* denotes the complex conjugate of any function a . $u_T(t)$ is $u(t)$ restricted to a time window of duration T . $\tilde{u}_T(f)$ is the Fourier transform of $u_T(t)$.

It is obvious to show that $S_{vu}(f)$ is just the complex conjugate of $S_{uv}(f)$. The power spectral density (PSD) of some stationary signal $u(t)$ is S_{uu} . It describes the energy contained in the signal $u(t)$ around the frequency f . Details on the calculation of the PSD and its statistical properties are provided in appendix A. We note that all the PSDs in this article are given in one-side power spectral densities, so the frequency is only positive.

To compute the Fourier transform of TDI variables, we should consider the atomic block in TDI formulation: the nested delay operator. We assume the light travel times are constants, i.e., $L_{ij}(t) = L_{ij}$. For a nested delay operator applied to a time series, $v(t) = \mathcal{D}_{i_1 i_2 \dots i_{n+1}} u(t)$, the Fourier transform is

$$\tilde{v}(\omega) = \exp \left(-j\omega \sum_{k=1}^n L_{i_k i_{k+1}} \right) \tilde{u}(\omega), \quad (14)$$

with n the number of delays.

The PSDs of the usual TDI generators (X, Y , and Z) are usually compositions of a limited set of patterns. For each term, we use (14) to form the Fourier transform and then compute the PSD.

We will use the shorthand notation

$$\bar{L}_{ij} = \frac{L_{ij} + L_{ji}}{2} \quad \text{and} \quad \bar{L}_{ijk} = \frac{L_{ij} + L_{ji} + L_{ik} + L_{ki}}{4} \quad (15)$$

Here, the PSD computation is done for the simple nested delay operator $\pm(1 - \mathcal{D}_{iji})u(t)$. The list of all useful patterns is provided in Table I.

$$\begin{aligned} \text{PSD} \quad & [\pm(1 - \mathcal{D}_{iji})u(t)](\omega) \\ & = \left\langle [(1 - \widetilde{\mathcal{D}}_{iji})u(t)](\omega) \times [(1 - \widetilde{\mathcal{D}}_{iji})u(t)]^*(\omega) \right\rangle \\ & = \left\langle \left(1 - e^{-j\omega(L_{ij} + L_{ji})}\right) \left(1 - e^{j\omega(L_{ij} + L_{ji})}\right) \tilde{u}(\omega) \tilde{u}^*(\omega) \right\rangle \\ & = 4 \sin^2(\omega \bar{L}_{ij}) S_u. \end{aligned} \quad (16)$$

The CSD computation have some common patterns. Note that we need to respect the order of the terms in the calculation.

1. $X = \pm(1 \pm \mathcal{D}_{iji})x(t)$ and $Y = \pm(1 \pm \mathcal{D}_{klk})u(t)$. We choose one case of specific set of signs in front of the nested delay operators, the others are easily

Nested delay operator	PSD
$\pm (1 - \mathcal{D}_{iji}) u(t)$	$4 \sin^2(\omega \bar{L}_{ij}) S_u$
$\pm (1 + \mathcal{D}_{iji}) u(t)$	$4 \cos^2(\omega \bar{L}_{ij}) S_u$
$\pm (1 - \mathcal{D}_{iji}) \mathcal{D}_{i_1 i_2 \dots i_n} u(t)$	$4 \sin^2(\omega \bar{L}_{ij}) S_u$
$\pm (1 + \mathcal{D}_{iji}) \mathcal{D}_{i_1 i_2 \dots i_n} u(t)$	$4 \cos^2(\omega \bar{L}_{ij}) S_u$
$\pm \mathcal{D}_{i_1 i_2 \dots i_n} (1 - \mathcal{D}_{iji}) u(t)$	$4 \sin^2(\omega \bar{L}_{ij}) S_u$
$\pm \mathcal{D}_{i_1 i_2 \dots i_n} (1 + \mathcal{D}_{iji}) u(t)$	$4 \cos^2(\omega \bar{L}_{ij}) S_u$
$\pm (1 + \mathcal{D}_{iji}) (1 - \mathcal{D}_{klk}) u(t)$	$16 \cos^2(\omega \bar{L}_{il}) \sin^2(\omega \bar{L}_{kl}) S_u$
$\pm (1 - \mathcal{D}_{iji}) (1 + \mathcal{D}_{klk}) u(t)$	$16 \sin^2(\omega \bar{L}_{ij}) \cos^2(\omega \bar{L}_{kl}) S_u$
$\pm (1 + \mathcal{D}_{iji}) (1 + \mathcal{D}_{klk}) u(t)$	$16 \cos^2(\omega \bar{L}_{ij}) \cos^2(\omega \bar{L}_{kl}) S_u$
$\pm (1 - \mathcal{D}_{iji}) (1 - \mathcal{D}_{klk}) u(t)$	$16 \sin^2(\omega \bar{L}_{ij}) \sin^2(\omega \bar{L}_{kl}) S_u$
$\pm (1 - \mathcal{D}_{iji} - \mathcal{D}_{ijiki} + \mathcal{D}_{ikijji}) u(t)$	$16 \sin^2(\omega \bar{L}_{ij}) \sin^2(2\omega \bar{L}_{ijk}) S_u$
$(a \pm b \mathcal{D}_{iji}) x(t)$	$[a^2 + b^2 \pm 2ab \cos(\omega \bar{L}_{ij})] S_u$

TABLE I. Table of PSD for the usual patterns present in TDI time domain formulations.

worked out in the same way.

B. Approximation justification

$$\begin{aligned}
CSD[X, Y] &= CSD[(1 - \mathcal{D}_{iji})u(t), (1 + \mathcal{D}_{klk})u(t)] \\
&= \left\langle [(1 - \widetilde{\mathcal{D}}_{iji})u(t)](\omega) \times [(1 + \widetilde{\mathcal{D}}_{klk})u(t)]^*(\omega) \right\rangle \\
&= \left\langle \left(1 - e^{-2j\omega \bar{L}_{ij}}\right) \left(1 + e^{2j\omega \bar{L}_{kl}}\right) \times \tilde{u}(\omega) \tilde{u}^*(\omega) \right\rangle \\
&= e^{j\omega(-\bar{L}_{ij} + \bar{L}_{kl})} \left(e^{j\omega \bar{L}_{ij}} - e^{-j\omega \bar{L}_{ij}} \right) \\
&\quad \times \left(e^{-j\omega \bar{L}_{kl}} + e^{j\omega \bar{L}_{kl}} \right) \langle \tilde{u}(\omega) \tilde{u}^*(\omega) \rangle \\
&= e^{j\omega(-\bar{L}_{ij} + \bar{L}_{kl})} 2j \sin(\omega \bar{L}_{ij}) 2j \cos(\omega \bar{L}_{kl}) S_u \\
&= -4 \sin(\omega \bar{L}_{ij}) \cos(\omega \bar{L}_{kl}) e^{j\omega(-\bar{L}_{ij} + \bar{L}_{kl})} S_u \quad (17)
\end{aligned}$$

2. $X = \pm(a \pm b \mathcal{D}_{iji})x(t)$ and $Y = \pm(1 \pm \mathcal{D}_{klk}) \mathcal{D}_{i_1 i_2 \dots i_n} u(t)$. We choose one case of specific set of signs in front of the nested delay operators, the others are easily worked out in the same way.

$$\begin{aligned}
CSD[X, Y] &= CSD[(a + b \mathcal{D}_{iji})u(t) * (1 - \mathcal{D}_{klk}) \mathcal{D}_{i_1 i_2 \dots i_n} u(t)] \\
&= \left\langle [(a + b \widetilde{\mathcal{D}}_{iji})u(t)](\omega) \right. \\
&\quad \left. \times [(1 - \widetilde{\mathcal{D}}_{klk}) \widetilde{\mathcal{D}}_{i_1 i_2 \dots i_n} u(t)]^*(\omega) \right\rangle \\
&= \left\langle \left(a + b e^{-j\omega(L_{ij} + L_{ji})} \right) \left(1 - e^{j\omega(L_{kl} + L_{lk})} \right) \right. \\
&\quad \left. \times e^{j\omega(L_{i_1} + L_{i_2} + \dots + L_{i_n})} \tilde{u}(\omega) \tilde{u}^*(\omega) \right\rangle \\
&= e^{j\omega(L_{i_1} + L_{i_2} + \dots + L_{i_n} - \bar{L}_{ij} + \bar{L}_{kl})} \left(e^{-j\omega \bar{L}_{kl}} - e^{j\omega \bar{L}_{kl}} \right) \\
&\quad \times \left(a e^{j\omega \bar{L}_{ij}} + b e^{-j\omega \bar{L}_{ij}} \right) \langle \tilde{u}(\omega) \tilde{u}^*(\omega) \rangle \\
&= -2j \sin(\omega \bar{L}_{kl}) e^{j\omega(L_{i_1} + L_{i_2} + \dots + L_{i_n} - \bar{L}_{ij} + \bar{L}_{kl})} \\
&\quad \times \left(a e^{j\omega \bar{L}_{ij}} + b e^{-j\omega \bar{L}_{ij}} \right) S_u. \quad (18)
\end{aligned}$$

In the previous subsections, some assumptions and approximations are made to reduce the complexity of the calculation. They are collected and justified here.

1. We assume that clock noise has been suppressed totally by the clock noise reduction algorithm [11]. Therefore we do not need to consider the sideband beams in our beam model, since they are only used for clock noise reduction. Since the residual clock noise is expected below secondary noises, this assumption is acceptable in our study case.
2. All measurements are perfectly synchronized in the barycentric coordinate time. Hence, there are no errors in time stamping the on-board measurements. This assumption simplifies the complexity of the computation.
3. All interferometric measurements are expressed as fractional frequency fluctuations around the nominal laser frequency. We assume this nominal laser frequency is constant and equal for all laser source, and it is equal to the nominal laser frequency, $c/1064 \text{ nm} = 282 \text{ THz}$.
4. The drag-free attitude control system (DFACS) is ignored in this study, which means the S/C and test-masses are treated as independent bodies. We also neglect the tilt-to-length coupling noise in the beam model.
5. We are assuming that S/C hardware from the noise performance perspective are statistically identical. Hence 6 test-mass acceleration noises have the same PSD, or a correlation noise appearing between two adjacent test-masses will occur similarly on all S/C.

6. All armlengths of the LISA constellation are constant, and so delay operators are commutative. We use this approximation frequently with unsuppressed noises because the armlength variation is a second-order effect for these noises. Therefore, this approximation is justified in the study of unsuppressed noises.

$$L_{ij}(t) = L_{ij} \quad \forall i, j \in \{1, 2, 3\} \quad (19)$$

7. Mostly in the case of unsuppressed noises, we neglect ranging and interpolation errors so the propagation delay operators and the TDI delay operators can be treated similarly, $\mathbf{D} \approx \mathcal{D}$. The effect of ranging and interpolation errors will contribute more significantly in the case of suppressed noises but this is out of the scope of this article.
8. To simplify the final transfer functions, we use the approximation of equal armlengths, which could be considered as the average armlength for long duration of the mission operation. Due to the almost equilateral configuration of the LISA constellation, we expect the average of each armlength should be not too different.

In the simulation validation studies (see Sec. III E), the 5 first approximations (no clock jitter noise, synchronized measurements, constant nominal laser frequency, no DFACS and noises of the same kind statistically similar) are made. The validity of these approximations will not be tested here, whereas it will be for approximations 6 to 8.

C. Procedure for spectral density computation

We will now detail the calculation of the transfer functions for unsuppressed noises, using as example test-mass acceleration noise. The propagation of other unsuppressed noises are worked out in a similar way.

The calculations are performed in several steps:

1. If we consider laser frequency planning, laser noises from the locking scheme should be substituted into the beam model⁶.
2. Since most of the time, we assume that noises of different types are uncorrelated, we can ignore all noises in the beams except for the one of interest. The LISA total noise transfer function is then simply the sum of all individual noise transfer functions. If a noise correlation scenario is considered,

we need to apply the correlation relations and keep only one of the correlated noises in the beam model.

3. Next step is the computation of TDI variables, presented in Sec. II G. First are the intermediary variables, then the TDI combinations. We write the result in terms of the product of nested delay operator applied to each noise, to ease the identification of patterns in the next step.
4. Hence, we can use the patterns PSD/CSD presented in Sec. III A for quick computation of the spectral density of individual noise terms. The noise terms are considered uncorrelated. The correlations are treated by introducing the same noise term in multiple measurements.
5. We use the approximation of constant armlengths (19) to simplify the computation (allowing to commute delay operators). Most of the time, the PSD XX and the CSD XY are enough because we can use index permutation to deduce the other spectral densities. This apply if the beams are symmetric, so it does not for the cases with frequency planning.
6. Finally, we sum up all components and simplify the result using some approximations presented in the end of Sec. III B.

D. A few examples

1. Uncorrelated test-mass acceleration noise without laser locking

In this section, we only consider test-mass acceleration noise. For simplicity, we omit the time dependency in the noise notation δ , but still remember that it is a time varying signal. We only consider the projection of test-mass displacement noise on the sensitive axis, δ_{ij} , since it is what enters the measurements.

Without frequency planning and correlation, the formulation of the measurements in S/C 1 are:

$$\begin{cases} \text{isi}_{12} = 0 \\ \text{rfi}_{12} = 0 \\ \text{tmi}_{12} = 2 \mathcal{F} \theta_{12}^{\text{rfi}} \delta_{12} \end{cases} \quad \begin{cases} \text{isi}_{13} = 0 \\ \text{rfi}_{13} = 0 \\ \text{tmi}_{13} = 2 \mathcal{F} \theta_{13}^{\text{rfi}} \delta_{13} \end{cases} \quad (20)$$

We then compute the TDI intermediary variables. We neglect the ranging and interpolation errors such that the two types of delay operators are equivalent, $\mathbf{D} \approx \mathcal{D}$. Moreover, the nominal laser wavelength for every laser source is constant and equal, i.e., $\lambda_{ij} = \lambda$. Applying these approximation to Eqs. (8), (9), (10) and (11), we get

$$\xi_{12} = -\theta_{12}^{\text{isi}} \mathcal{F} (\mathcal{D}_{12} \delta_{21} + \delta_{12}), \quad (21)$$

$$\xi_{13} = -\theta_{13}^{\text{isi}} \mathcal{F} (\mathcal{D}_{13} \delta_{31} + \delta_{13}), \quad (22)$$

⁶ An alternative approach is shown in Sec. 12.2 of [10]. In principle, TDI makes sure all the p_{ij} terms are strongly suppressed, so any secondary noise terms in p_{ij} due to laser locking are suppressed alongside the laser noise. Therefore, we expect the secondary noise levels to remain identical regardless of the locking scheme, as verified by the explicit computation.

and then

$$\eta_{12} = -\mathcal{F}(\mathcal{D}_{12}\delta_{21} + \delta_{12}), \quad (23)$$

$$\eta_{13} = -\mathcal{F}(\mathcal{D}_{13}\delta_{31} + \delta_{13}). \quad (24)$$

The Michelson combination is computed as follows, using the constant armlength approximation (19) (we can commute the delay operators with themselves and with antialiasing filter operator⁷).

$$\begin{aligned} X_2 &= (1 - \mathcal{D}_{12131})[(\eta_{13} + \mathcal{D}_{13}\eta_{31}) \\ &\quad + \mathcal{D}_{131}(\eta_{12} + \mathcal{D}_{12}\eta_{21})] - (1 - \mathcal{D}_{13121}) \\ &\quad \times [(\eta_{12} + \mathcal{D}_{12}\eta_{21}) + \mathcal{D}_{121}(\eta_{13} + \mathcal{D}_{13}\eta_{31})] \\ &\approx (1 - \mathcal{D}_{12131})[(1 - \mathcal{D}_{121})(\eta_{13} + \mathcal{D}_{13}\eta_{31}) \\ &\quad - (1 - \mathcal{D}_{131})(\eta_{12} + \mathcal{D}_{12}\eta_{21})] \\ &= \mathcal{F}\left\{ \begin{aligned} &-(1 - \mathcal{D}_{12131})(1 - \mathcal{D}_{121})(1 + \mathcal{D}_{131})\delta_{13} \\ &-2(1 - \mathcal{D}_{12131})(1 - \mathcal{D}_{121})\mathcal{D}_{13}\delta_{31} \\ &+(1 - \mathcal{D}_{12131})(1 - \mathcal{D}_{131})(1 + \mathcal{D}_{121})\delta_{12} \\ &+2(1 - \mathcal{D}_{12131})(1 - \mathcal{D}_{131})\mathcal{D}_{12}\delta_{21} \end{aligned} \right\} \quad (25) \end{aligned}$$

The Y -channel is just the index permutation of X -channel.

$$\begin{aligned} Y_2 &= \mathcal{F}\left\{ \begin{aligned} &-(1 - \mathcal{D}_{23212})(1 - \mathcal{D}_{232})(1 + \mathcal{D}_{212})\delta_{21} \\ &-2(1 - \mathcal{D}_{23212})(1 - \mathcal{D}_{232})\mathcal{D}_{21}\delta_{12} \\ &+(1 - \mathcal{D}_{23212})(1 - \mathcal{D}_{212})(1 + \mathcal{D}_{232})\delta_{23} \\ &+2(1 - \mathcal{D}_{23212})(1 - \mathcal{D}_{212})\mathcal{D}_{23}\delta_{32} \end{aligned} \right\} \quad (26) \end{aligned}$$

The PSD of these Michelson variables can be worked out by collecting the Fourier transforms of the auto-correlation functions of each noise in each MOSA. Assuming uncorrelated noises, the cross-terms between two different noises, such as $\langle \widetilde{\delta}_{12}^*(f)\widetilde{\delta}_{13}(f) \rangle$, are vanishing. We can also use results from Sec. III A for fast deduction. For example, the contribution to the PSD of X -channel $S_{XX}(f)$ of acceleration noise in MOSA 13 reads:

$$\begin{aligned} &\text{PSD}[-\mathcal{F}(1 - \mathcal{D}_{12131})(1 - \mathcal{D}_{121})(1 + \mathcal{D}_{131})\delta_{13}](\omega) \\ &= 64S_{\mathcal{F}}(\omega)S_{\delta_{13}}(\omega)\sin^2[\omega(\bar{L}_{12} + \bar{L}_{31})] \\ &\quad \times \sin^2(\omega\bar{L}_{12})\cos^2(\omega\bar{L}_{31}), \quad (27) \end{aligned}$$

where $S_{\mathcal{F}}(\omega) = \langle |\tilde{\mathcal{F}}(f)|^2 \rangle$ and $S_{\delta_{13}}(\omega) = \langle |\widetilde{\delta}_{13}(f)|^2 \rangle$. Then, one can check that the PSD of the X -channel for

the uncorrelated test-mass acceleration noise is

$$\begin{aligned} S_{XX}^{\text{uncorr acc tm}}(\omega) &= 64S_{\mathcal{F}}(\omega)\sin^2[\omega(\bar{L}_{12} + \bar{L}_{31})] \\ &\quad \times \left\{ \begin{aligned} &\sin^2(\omega\bar{L}_{12})[\cos^2(\omega\bar{L}_{31})S_{\delta_{13}}(\omega) \\ &+ S_{\delta_{31}}(\omega)] + \sin^2(\omega\bar{L}_{31}) \\ &\times [\cos^2(\omega\bar{L}_{12})S_{\delta_{12}}(\omega) + S_{\delta_{21}}(\omega)] \end{aligned} \right\} \quad (28) \end{aligned}$$

The PSD of Y -channel, $S_{YY}^{\text{uncorr acc tm}}$, has the same form with permuted indices $\{1 \rightarrow 2, 2 \rightarrow 3, 3 \rightarrow 1\}$. We can use the equal armlength approximations $L_{ij} = L$ and that all test-mass acceleration noises share the same PSD, $S_{\delta_{ij}} = S_{\delta}$, to get:

$$\begin{aligned} S_{XX}^{\text{uncorr acc tm}}(\omega) &= S_{YY}^{\text{uncorr acc tm}}(\omega) \\ &= 64\sin^2(2\omega L)\sin^2(\omega L)[3 + \cos(2\omega L)] \\ &\quad \times S_{\mathcal{F}}(\omega)S_{\delta}(\omega) \quad (29) \end{aligned}$$

To compute the CSD between X and Y , we use the same procedure and collect the nonzero terms that have the same noise index. Note that $CSD[Y, X] = CSD[X, Y]^*$, so we only need to compute the CSD of XY . We can also use the CSD result from Sec. III A. For example, the contribution of acceleration noise in MOSA 12 to the CSD S_{XY} reads:

$$\begin{aligned} &\text{CSD}\left[\mathcal{F}(1 - \mathcal{D}_{12131})(1 - \mathcal{D}_{131})(1 + \mathcal{D}_{121})\delta_{12} \right. \\ &\quad \left. * (-2)(1 - \mathcal{D}_{23212})(1 - \mathcal{D}_{232})\mathcal{D}_{21}\delta_{12}\right](\omega) \\ &= -64S_{\mathcal{F}}(\omega)S_{\delta_{12}}(\omega)\sin[\omega(\bar{L}_{12} + \bar{L}_{31})] \\ &\quad \times \sin[\omega(\bar{L}_{12} + \bar{L}_{23})]\sin(\omega\bar{L}_{13})\sin(\omega\bar{L}_{23})\cos(\omega\bar{L}_{12}) \\ &\quad \times \exp[-j\omega(2\bar{L}_{13} - 2\bar{L}_{23} + \bar{L}_{12} - L_{21})] \quad (30) \end{aligned}$$

One can find the CSD of XY is given by

$$\begin{aligned} S_{XY}^{\text{uncorr acc tm}}(\omega) &= -64S_{\mathcal{F}}(\omega)\sin[\omega(\bar{L}_{12} + \bar{L}_{31})] \\ &\quad \times \sin[\omega(\bar{L}_{12} + \bar{L}_{23})]\sin(\omega\bar{L}_{13}) \\ &\quad \times \sin(\omega\bar{L}_{23})\cos(\omega\bar{L}_{12})e^{-j\omega\frac{L_{12}-L_{21}}{2}} \\ &\quad \times e^{-2j\omega(\bar{L}_{13}-\bar{L}_{23})}[S_{\delta_{12}}(\omega) + S_{\delta_{21}}(\omega)] \quad (31) \end{aligned}$$

Assuming equal armlengths and the same test-mass acceleration noise level in all MOSAs, we obtain

$$S_{XY}^{\text{uncorr acc tm}}(\omega) = -64S_{\mathcal{F}}(\omega)\sin^3(2\omega L)\sin(\omega L)S_{\delta}(\omega) \quad (32)$$

2. Uncorrelated test-mass acceleration noise with laser locking

To account for frequency planning, we need to derive the locked laser frequency fluctuations as functions of

⁷ This is not true in the case of suppressed noises like laser frequency noise. In such cases, we need to take into account the noncommutation of delay operators with themselves and with filter operators [12].

the primary laser, p_{32} , before substituting them in the beam model and interferometric measurements. We use the group of equations (7) and we only keep track of the test-mass acceleration and primary laser noises,

$$p_{23} = \mathbf{D}_{12} p_{32} \quad (33a)$$

$$p_{31} = p_{32} \quad (33b)$$

$$p_{13} = \mathbf{D}_{21} p_{32} \quad (33c)$$

$$p_{12} = \mathbf{D}_{21} p_{32} \quad (33d)$$

$$p_{21} = \mathbf{D}_{321} p_{32}. \quad (33e)$$

Due to laser locking, the beams and interferometric measurements are no longer symmetric for the different S/C. We therefore give the interferometric signals for the whole LISA constellation

- On S/C 1:

$$\begin{cases} \text{isi}_{12} &= \theta_{12}^{\text{isi}} \mathcal{F} (\mathbf{D}_{121} - 1) \mathbf{D}_{13} p_{32} \\ \text{rfi}_{12} &= 0 \\ \text{tmi}_{12} &= 2 \mathcal{F} \theta_{12}^{\text{rfi}} \delta_{12} \end{cases} \quad (34)$$

$$\begin{cases} \text{isi}_{13} &= 0 \\ \text{rfi}_{13} &= 0 \\ \text{tmi}_{13} &= 2 \mathcal{F} \theta_{13}^{\text{rfi}} \delta_{13} \end{cases} \quad (35)$$

- On S/C 2:

$$\begin{cases} \text{isi}_{23} &= 0 \\ \text{rfi}_{23} &= \theta_{23}^{\text{rfi}} \mathcal{F} (\mathbf{D}_{213} - \mathbf{D}_{23}) p_{32} \\ \text{tmi}_{23} &= \theta_{23}^{\text{rfi}} \mathcal{F} [(\mathbf{D}_{213} - \mathbf{D}_{23}) p_{32} + 2\delta_{23}] \end{cases} \quad (36)$$

$$\begin{cases} \text{isi}_{21} &= 0 \\ \text{rfi}_{21} &= \theta_{21}^{\text{rfi}} (\mathbf{D}_{23} - \mathbf{D}_{213}) p_{32} \\ \text{tmi}_{21} &= \theta_{21}^{\text{rfi}} \mathcal{F} [(\mathbf{D}_{23} - \mathbf{D}_{213}) p_{32} + 2\delta_{21}] \end{cases} \quad (37)$$

- On S/C 3:

$$\begin{cases} \text{isi}_{31} &= \theta_{31}^{\text{isi}} (\mathbf{D}_{313} - 1) p_{32} \\ \text{rfi}_{31} &= 0 \\ \text{tmi}_{31} &= 2\mathcal{F} \theta_{31}^{\text{rfi}} \delta_{31} \end{cases} \quad (38)$$

$$\begin{cases} \text{isi}_{32} &= \theta_{32}^{\text{isi}} (\mathbf{D}_{323} - 1) p_{32} \\ \text{rfi}_{32} &= 0 \\ \text{tmi}_{32} &= 2\mathcal{F} \theta_{32}^{\text{rfi}} \delta_{32} \end{cases} \quad (39)$$

The next step is to compute the TDI intermediary vari-

ables ξ, η . Assuming $\mathbf{D} = \mathcal{D}$, one can verify that

$$\eta_{12} = \mathcal{F} (\mathcal{D}_{123} - \mathcal{D}_{13}) p_{32} - \mathcal{F} (\mathcal{D}_{12} \delta_{21} + \delta_{12}) \quad (40)$$

$$\eta_{13} = -\mathcal{F} (\mathcal{D}_{13} \delta_{31} + \delta_{13}) \quad (41)$$

$$\eta_{23} = -\mathcal{F} (\mathcal{D}_{23} \delta_{32} + \delta_{23}) \quad (42)$$

$$\eta_{21} = \mathcal{F} (\mathcal{D}_{213} - \mathcal{D}_{23}) p_{32} - \mathcal{F} (\mathcal{D}_{21} \delta_{12} + \delta_{21}) \quad (43)$$

$$\eta_{31} = \mathcal{F} (\mathcal{D}_{313} - 1) p_{32} - \mathcal{F} (\mathcal{D}_{31} \delta_{13} + \delta_{31}) \quad (44)$$

$$\eta_{32} = \mathcal{F} (\mathcal{D}_{323} - 1) p_{32} - \mathcal{F} (\mathcal{D}_{32} \delta_{23} + \delta_{32}) \quad (45)$$

We note that, except for the terms with laser frequency noise p_{32} , all terms in η are identical to the case without laser locking. That is expected because the locking constraints (7) do not contain test-mass acceleration noise in any term. The X -channel for laser noise only is

$$X_2^{\text{p-only}} = \mathcal{F} [(1 - \mathcal{D}_{13121})(1 - \mathcal{D}_{12131}) - (1 - \mathcal{D}_{12131})(1 - \mathcal{D}_{13121})] p_{32}, \quad (46)$$

which is canceled out when we commute the TDI delay, i.e., using constant delays assumption. In the end, the TDI combinations X, Y and Z in the case of laser locking for the test-mass acceleration noise are exactly the same as in the case without laser locking, (29) and (32).

3. Uncorrelated readout and optical path noises with laser locking

The locking constraints (7) contain readout noises, $N_{x,ij}^{ro}$, and optical path noises, $N_{loc/x,ij}^{op}$. Therefore, the situation is different from acceleration noise. Expanding η_{12} without laser locking, we get:

$$\eta_{12} = \theta_{21}^{\text{isi}} \mathcal{F} N_{s,12}^{ro} - \theta_{21}^{\text{rfi}} \mathcal{F} \mathcal{D}_{12} \frac{N_{\epsilon,21}^{ro} - N_{\text{rfi},21}^{ro}}{2} - \theta_{12}^{\text{rfi}} \mathcal{F} \frac{N_{\epsilon,12}^{ro} - N_{\text{rfi},12}^{ro}}{2} + \theta_{21}^{\text{rfi}} \mathcal{D}_{12} \mathcal{F} \frac{N_{\text{rfi},21}^{ro} + N_{\text{rfi},23}^{ro}}{2}, \quad (47)$$

while we get with laser locking:

$$\eta_{12} = \theta_{12}^{\text{isi}} \mathcal{F} N_{s,12}^{ro} - \theta_{21}^{\text{rfi}} \mathcal{D}_{12} \mathcal{F} \frac{N_{\epsilon,21}^{ro} - N_{\text{rfi},21}^{ro}}{2} - \theta_{12}^{\text{rfi}} \mathcal{F} \frac{N_{\epsilon,12}^{ro} - N_{\text{rfi},12}^{ro}}{2} + \theta_{21}^{\text{rfi}} \mathcal{D}_{12} \mathcal{F} \frac{N_{\text{rfi},21}^{ro} + N_{\text{rfi},23}^{ro}}{2} - \theta_{13}^{\text{isi}} \mathcal{F} N_{s,13}^{ro} + \theta_{23}^{\text{isi}} \mathcal{F} \mathcal{D}_{12} N_{s,23}^{ro} - \theta_{31}^{\text{rfi}} \mathcal{F} \mathcal{D}_{13} N_{\text{rfi},31}^{ro} - \theta_{12}^{\text{rfi}} \mathcal{F} N_{\text{rfi},12}^{ro} \quad (48)$$

We observe that laser locking introduces additional terms. These terms actually vanish at the next TDI step, when forming the variable η . Considering, for example, solely $N_{s,13}^{ro}$, we have

$$\eta_{12} = -\theta_{13}^{\text{isi}} N_{s,13}^{ro},$$

$$\eta_{21} = \theta_{13}^{\text{isi}} \mathcal{D}_{21} N_{s,13}^{ro},$$

$$\eta_{31} = \theta_{13}^{\text{isi}} \mathcal{D}_{31} N_{s,13}^{ro}$$

Substituting in X_2 given by Eq. (12), we get

$$X_2 = [1 - \mathcal{D}_{121} - \mathcal{D}_{12131} + \mathcal{D}_{1312121} + (\mathcal{D}_{13121} - \mathcal{D}_{12131}) + (\mathcal{D}_{131212131} - \mathcal{D}_{121313121})] \theta_{13}^{\text{isi}} N_{s,13}^{\text{ro}}. \quad (49)$$

Assuming that delay operators commute, the terms in parentheses disappear and we are back to the results without laser locking.

One can checked that we obtain the same results as for the case without laser locking, for all terms of readout noises and optical path noises. Finally, we find that the results are the same with and without laser locking for all unsuppressed noises.

4. Correlated acceleration noise

Finally, we consider the correlation scenario (5) for test-mass acceleration noise. The correlation relation is

$$\delta_{ij} = \gamma \delta_{ik}, \quad (50)$$

for $(i, j, k) =$ circular permutation of $(1, 2, 3)$, with γ the correlation factor and with $j \neq k$. We substitute this in the beam model and then form the interferometric measurements. Since the correlated noises are in the same S/C, the interferometric measurements remain symmetric (as in the uncorrelated noise case). In S/C 1, we keep only the test-mass acceleration noise from MOSA 12,

$$\begin{cases} \text{isi}_{12} = 0 \\ \text{rfi}_{12} = 0 \\ \text{tmi}_{12} = 2 \mathcal{F} \theta_{12}^{\text{rfi}} \delta_{12} \end{cases} \quad \begin{cases} \text{isi}_{13} = 0 \\ \text{rfi}_{13} = 0 \\ \text{tmi}_{13} = 2 \mathcal{F} \theta_{13}^{\text{rfi}} \gamma \delta_{12} \end{cases} \quad (51)$$

Then, the TDI intermediary variables η for S/C 1 are

$$\eta_{12} = -\mathcal{F}(\gamma \mathcal{D}_{12} \delta_{23} + \delta_{12}), \quad (52)$$

$$\eta_{13} = -\mathcal{F}(\mathcal{D}_{13} \delta_{31} + \gamma \delta_{12}) \quad (53)$$

Applying the same procedure as for the uncorrelated case, we get the following expression for the PSD:

$$S_{\text{XX}}^{\text{corr acc tm}}(\omega) = 32 \left[3\gamma^2 + 2\gamma + 3 + (1 + \gamma)^2 \cos(2\omega L) \right] \times \sin^2(2\omega L) \sin^2(\omega L) S_{\mathcal{F}}(\omega) S_{\delta}(\omega), \quad (54)$$

and, for the CSD,

$$S_{\text{XY}}^{\text{corr acc tm}}(\omega) = -64 \left[(1 + \gamma)^2 \cos(2\omega L) - \gamma \right] \times \sin^2(2\omega L) \sin^2(\omega L) S_{\mathcal{F}}(\omega) S_{\delta}(\omega) \quad (55)$$

This example is a good illustration of the importance of correlation. Indeed, at low frequency, $\cos(2\omega L) \sim 1$, and the fully correlated case ($\gamma = 1$) is 1.5 times higher than the uncorrelated case. On the other hand, the fully anticorrelated case ($\gamma = -1$) case is 2 times lower than the uncorrelated case.

E. Validation with simulation

1. LISANode

LISANode [29] is the current official simulator of the LISA Consortium. It is a time domain simulator based on a modular structure using graphs to connect blocks and finally core components. The core components are coded in **C++** and the rest (organization of components, graph building and validation, user interface) is in **Python**. Part of the logic and several elements are inherited from the **LISACode** simulator [6, 25]. **LISANode** takes as inputs an orbit file, a frequency plan and potentially GW files and glitch files. It simulates the noises sources, the propagation of laser beams, the interferometric measurements, the phasometers, the clocks, etc. It produces the interferometric measurements at 16 Hz. These measurements are then filtered and downsampled at 4 Hz to produce the telemetered data. The simulator is then connected to a processing module to apply TDI and produce any TDI variables. It has already been used in multiple studies [11–13, 15] and is described in [8, 10].

2. Numerical method for spectral estimation

The procedure to validate the transfer function of a particular type of noise (for example acceleration noise or readout noise) is the following:

- i) We configure the simulation for the noise to be studied, with all other noises configured to produce zeros as output;
- ii) From the simulated time domain data, we compute the PSD and the CSD;
- iii) For the same set of frequencies, we compute data from our analytical formulation;
- iv) We overplot the simulated and analytical PSDs or CSDs, adding for the analytical curve, the 99.73% confidence interval (3σ for normal distribution) which is computed statistically for our Welch PSD/CSD estimates;
- v) The simulated points outside the confidence interval are detected. The level of agreement between analytical formulation and simulated data is estimated based on the plot and the number of points outside the confidence interval.

IV. RESULTS

A. Propagation of unsuppressed noises

1. Analytical formulations

To summarize all analytical results, we list the noises with the specific correlation and the TDI transfer func-

tions for X in Table II. The results are the same for Y and Z , even with laser locking. For all these results, the equal armlengths and equal noise level approximations are used. We do not distinguish between the case with or without laser locking, since the results are identical for the unsuppressed noises. For the sake of brevity, we introduce two common factors in the summary table:

$$C_{XX}(\omega) = 16 \sin^2(\omega L) \sin^2(2\omega L), \quad (56)$$

$$C_{XY}(\omega) = -16 \sin(\omega L) \sin^3(2\omega L). \quad (57)$$

Several types of noises share the same transfer function. For some of them, it is simply because the noises enter identically in the measurement (e.g., readout ISI and optical path ISI).

As a result, we recover the transfer functions of all common noises existing in LISA sensitivity [2] after using the approximations. New transfer functions of the optical path and readout noises in test-mass interferometers are found, which can change the shape of LISA sensitivity. In different noise correlation scenarios, the transfer functions could be either lower or higher than the ones in the uncorrelated case, which can help build the worst-case model for the LISA noise budget.

There is another set of TDI variables, called A, E, T , constructed from X, Y, Z [30, 31]:

$$A = \frac{Z - X}{\sqrt{2}}, \quad E = \frac{X - 2Y + Z}{\sqrt{6}}, \quad T = \frac{X + Y + Z}{\sqrt{3}}. \quad (58)$$

A, E, T are useful for data analysis since they have vanishing CSDs under the approximations of equal arm-lengths and equal noise levels for the same type noises. The PSDs for A, E, T are given in Table III. They combine the PSDs and CSDs of X, Y, Z as

$$S_{AA} = \frac{S_{ZZ} + S_{XX} - 2\text{Re}[S_{ZX}]}{2} \quad (59)$$

$$S_{EE} = \frac{S_{XX} + 4S_{YY} + S_{ZZ} - 2\text{Re}[2S_{XY} - S_{XZ} + 2S_{YZ}]}{6} \quad (60)$$

$$S_{TT} = \frac{S_{XX} + S_{YY} + S_{ZZ} + 2\text{Re}[S_{XY} + S_{XZ} + S_{YZ}]}{3} \quad (61)$$

and are therefore slightly more complex. We remark that while the equal arm models derived here are accurate enough to describe the GW-sensitive channels X, Y, Z , as well as for the quasiorthogonal channels A and E , it was demonstrated that this assumption is insufficient for accurately describing the behavior of the null channel T , in particular at low frequencies [32, 33].

2. Analytic formulations versus simulations

For the frequency range 10^{-4} to 1 Hz, the simulated and analytical PSD/CSD for TDI X have been plotted

(see Figs. 4, 5, 6 and 7). Red lines show the analytical formulation expressions. The blue dashed lines represent the instrument response to the simulated single noises (i.e., the test-mass acceleration noise in the following example) for a duration about 3×10^5 s for uncorrelated and correlated cases and about 7×10^4 s for anticorrelated case. The green envelope highlights the 99.73% confidence interval with respect to the analytical formulation. The width of the envelope depends on the confidence interval and on the duration of the simulation (see the difference between 6 and 4 and 5). The probability that a single point is outside of the confidence interval is around 4.5×10^{-7} in case of a perfect agreement between analytical formulation and simulation (see appendix A and Eq. A5).

Figures 4, 5, and 6 show a great agreement for the test-mass acceleration noise PSD in all uncorrelated, correlated and anticorrelated cases.

The confidence interval described in the appendix A is not applicable to the CSD. Nevertheless, the CSD computation shows good visual agreement with the simulated data from LISANode (see figure 7).

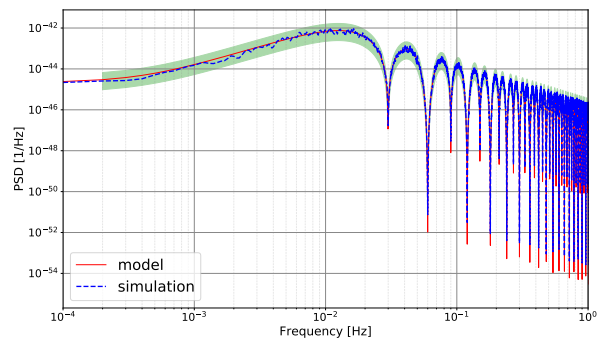


FIG. 4. Uncorrelated test-mass acceleration noise cross-comparison. The simulated data (red line) at 99.73% confidence interval (green area) are in great agreement with the analytical formulation (blue dashed line).

B. About the propagation of suppressed noises

Although this article focuses on unsuppressed noises, for the sake of completeness, we will summarize the status of transfer functions for the suppressed noises, i.e., noises suppressed by TDI, as well as the additional noises induced by this suppression.

Laser frequency noise has to be suppressed by several order of magnitude by TDI, in order to be below the required noise level [2, 24, 31] defined by the unsuppressed noises (acceleration, readout and optical path). It has been the main focus of TDI noise reduction studies during many years, one of the most recent studies on

Noise type	Correlation	PSD	CSD
test-mass acceleration	None	$4C_{XX}(\omega) [3 + \cos(2\omega L)]$	$4C_{XY}(\omega)$
	Correlated noises at the same S/C	$8C_{XX}(\omega)$	$-4C_{XX}(\omega)$
	Anticorrelated noises at the same S/C	$8C_{XX}(\omega) [2 + \cos(2\omega L)]$	$4C_{XX}(\omega) [1 - 4\cos(\omega L)]$
Readout (TMI) and Optical Pathlength (TMI)	None	$C_{XX}(\omega) [3 + \cos(2\omega L)]$	$C_{XY}(\omega)$
	Correlated adjacent TMI noise	$2C_{XX}(\omega)$	$-C_{XX}(\omega)$
	Anticorrelated adjacent TMI noise	$2C_{XX}(\omega) [2 + \cos(2\omega L)]$	$C_{XX}(\omega) [1 - 4\cos(\omega L)]$
Backlink (TMI)	None	$C_{XX}(\omega) [3 + \cos(2\omega L)]$	$C_{XY}(\omega)$
Readout (ISI and RFI) and Optical Pathlength (ISI and RFI)	None	$4C_{XX}(\omega)$	$C_{XY}(\omega)$
	Correlated adjacent IFO noise	$2C_{XX}(\omega)$	$-C_{XX}(\omega)$
	Anticorrelated adjacent IFO noise	$6C_{XX}(\omega)$	$C_{XX}(\omega) [1 - 4\cos(\omega L)]$
	Correlated noises at the same telescope	$4C_{XX}(\omega) [3 + \cos(2\omega L)]$	$4C_{XY}(\omega)$
Backlink (RFI)	None	$4C_{XX}(\omega)$	$C_{XY}(\omega)$

TABLE II. Summary table of analytical TDI X, Y, Z transfer functions for unsuppressed noises. All results have been simplified using approximations (refer to Sec. III B).

Noise type	Correlation	PSD A & E	PSD T
test-mass acceleration	None	$4C_{XX}(\omega) [3 + 2\cos(\omega L) + \cos(2\omega L)]$	$32C_{XX}(\omega) \sin^4(\frac{\omega L}{2})$
	Correlated noises at the same S/C	$12C_{XX}(\omega)$	0
	Anticorrelated noises at the same S/C	$4C_{XX}(\omega) [1 + 2\cos(\omega L)]^2$	$64C_{XX}(\omega) \sin^4(\frac{\omega L}{2})$
Readout (TMI) and Optical Pathlength (TMI)	None	$C_{XX}(\omega) [3 + 2\cos(\omega L) + \cos(2\omega L)]$	$8C_{XX}(\omega) \sin^4(\frac{\omega L}{2})$
	Correlated adjacent TMI noise	$3C_{XX}(\omega)$	0
	Anticorrelated adjacent TMI noise	$C_{XX}(\omega) [1 + 2\cos(\omega L)]^2$	$16C_{XX}(\omega) \sin^4(\frac{\omega L}{2})$
Backlink (TMI)	None	$C_{XX}(\omega) [3 + 2\cos(\omega L) + \cos(2\omega L)]$	$8C_{XX}(\omega) \sin^4(\frac{\omega L}{2})$
Readout (ISI and RFI) and Optical Pathlength (ISI and RFI)	None	$2C_{XX}(\omega) [2 + \cos(\omega L)]$	$4C_{XX}(\omega) [1 - \cos(\omega L)]$
	Correlated adjacent IFO noise	$3C_{XX}(\omega)$	0
	Anticorrelated adjacent IFO noise	$C_{XX}(\omega) [5 + 4\cos(\omega L)]$	$-8C_{XX}(\omega) [-1 + \cos(\omega L)]$
	Correlated noises at the same telescope	$4C_{XX}(\omega) [3 + 2\cos(\omega L) + \cos(2\omega L)]$	$32C_{XX}(\omega) \sin^4(\frac{\omega L}{2})$
Backlink (RFI)	None	$2C_{XX}(\omega) [2 + \cos(\omega L)]$	$4C_{XX}(\omega) [1 - \cos(\omega L)]$

TABLE III. Summary table of analytical TDI A, E, T transfer functions for unsuppressed noises. All results have been simplified using approximations (refer to Sec. III B).

the topic being [12]. Because of the high level of reduction required, the residual level is sensitive to all limiting effects from the application of TDI: flexing-filtering (noncommutation between antialiasing filters and delays) [12], ranging bias, stochastic ranging (imprecision in the knowledge of delays), interpolation, aliasing and fundamental armlength mismatch (limitation due to the flexing with TDI 2.0). There are ongoing active studies on all these effects and preliminary transfer functions are already available enabling to establish the expected level of the residual laser noise. Moreover, the residual laser noise depends on the laser locking configuration. Only preliminary checks based on simulation have been done

and preliminary models have been developed [10], and more detailed studies are necessary.

In principle, most effects leading to residual laser noise will also cause residuals in other noise sources which are perfectly canceled in an idealized situation. However, since these other suppressed noises are several orders of magnitude smaller than laser noise, their residuals can usually be neglected.

Clock noise is also reduced by TDI. While its initial level is lower than that of laser noise, it is still a few orders of magnitude higher than the required noise level. In order to suppress clock noise, the laser beams carry sideband modulation with a clock-derived signal, creating

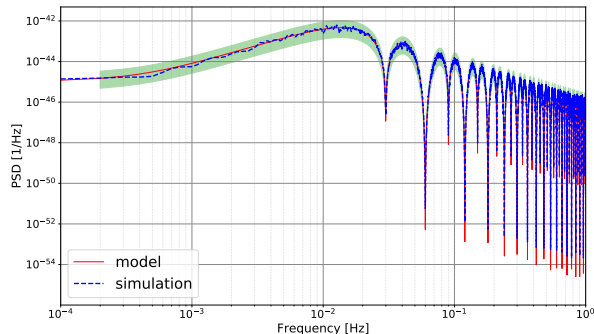


FIG. 5. Correlated test-mass acceleration noise cross-comparison. The simulated data (red line) at 99.73% confidence interval (green area) are in great agreement with the analytical formulation (blue dashed line).

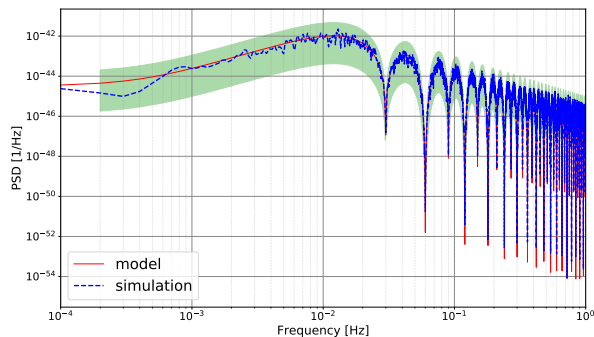


FIG. 6. Anticorrelated test-mass acceleration noise cross-comparison. The simulated data (red line) at 99.73% confidence interval (green area) are in great agreement with the analytical formulation (blue dashed line).

so-called clock-sidebands. Interferometric measurements of these sidebands are then used in the TDI algorithm to reduce clock noise [11].

S/C jitter noises $\vec{\Delta}_{ij}$ are in theory perfectly canceled by TDI when forming the ξ_{ij} (see (8) and (9)). In reality, this cancellation will not be perfect and some residual noise is expected.

Finally, since the application of TDI is a numerical procedure, some numerical limitations are expected.

The estimated residuals of all suppressed noises are currently below the required level, but some contributions are not negligible and need to be carefully studied. The laser locking will impact some of these suppressed noises and is the topic of further studies currently underway.

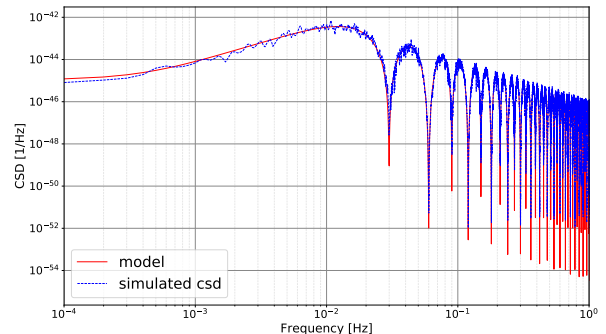


FIG. 7. CSD uncorrelated TM acceleration noise. The red line is the simulated data and the blue dashed line is the analytical formulation.

V. CONCLUSION

The modeling of the noises and their propagation from the measurements to the TDI variables are crucial for the LISA mission. Indeed, the TDI algorithm will reduce some noise sources while leaving others largely untouched. The impact of correlations between links can either improve or deteriorate the performance of the mission at the TDI level. We have seen this in the particular case of test mass acceleration noise, but it is also true for tilt-to-length [14] or thermo-mechanical noises. In addition, many noises related to the application of the algorithm itself, such as interpolation, clock noise residual or sideband modulation noise [11] can only be expressed at TDI level. Whether it is to establish the noise budget of the mission or to improve our understanding and knowledge of the noise for the needs of data analysis, the use of these TDI models is necessary.

The TDI variables are the main data used to extract GW signals. Therefore, it is important to have a good modeling of the noise PSD and CSD for the various TDI variables in order to search for GW sources, estimate their parameters and distinguish them from the instrument noises. This last point is particularly important for the search for stochastic gravitational wave backgrounds which can easily be confused with noise.

In this article, we revisit a method to compute analytically the PSDs and the CSDs of unsuppressed noises at TDI level, as well as justify the approximations to simplify the result. We indeed derive the TDI transfer functions for most of noises in the update model for the LISA interferometric measurements in the more realistic configuration. We recover the transfer functions of the standard LISA unsuppressed noises [2, 3, 26] in the ideal case, i.e., under the assumption of equal armlengths and identical statistical properties of same type noises in different MOSAs. It also turns out that the optical and readout noises in the test-mass interferometers have different transfer function than the ones in reference and

intersatellite interferometers.

In addition, some standard cases of correlation have been studied. Accordingly, the spectral density of correlated noises could either improve or degrade the LISA noise budget, depending whether they are anticorrelated or fully correlated. Further analyses to identify correlation scenario preferable in reality are required.

The analytical expressions are provided in Tables II and III for the TDI variables X, Y, Z, A, E , and T . The analytical transfer functions of X, Y, Z have been validated against simulations in different configurations.

The same method can be applied to any unsuppressed noises and to any TDI variables.

The transfer functions for the unsuppressed noises with laser locking are the same as the ones without laser locking. It is not necessarily the case for suppressed noises, but we leave this for future works. Actually the propagation of suppressed noises is usually more complicated. Several studies are underway and should soon result in publications.

Appendix A: Estimation of power spectral densities

In the following we describe the procedure of estimating the power spectral density for a stochastic time series $x(t)$ of finite length T . We use the Scipy implementation of the so-called ‘‘Welch’s method’’. It is summarized in the following steps. First, the data is divided into M segments of length L and a window function $w(t)$ is applied. Then, for each segment the Fourier transform is calculated which form independent estimates of the power spectral density as defined in (A1). Finally, the average [see (A2)] over the M segments is taken to reduce the variance.

$$\hat{S}^{(m)}(f_k) = \frac{|\tilde{x}_w^{(m)}(f_k)|^2}{L} \quad (\text{A1})$$

$$\bar{S}(f_k) = \frac{1}{M} \sum_{m=0}^{M-1} \hat{S}^{(m)}(f_k) \quad (\text{A2})$$

This procedure yields estimates of $\bar{S}(f_k)$ at frequencies $f_k = \Delta f k$ with k running from zero to $K = L f_s$. The spectral resolution is given by $\Delta f = \frac{1}{L}$. In theory one could choose to average over many segments to yield a very precise estimate of the PSD. However, in reality we are faced with limited amount of data and have to trade off between low variance and high spectral resolution.

In our studies we aim to validate the analytical PSD models with simulated data. To check whether the PSD

estimates $\bar{S}(f_k)$ are consistent with the model (null hypothesis) we conduct an hypothesis test. We define the confidence level γ that represents the probability that all PSD estimates are inside a given confidence interval.

$$\gamma = \prod_k^{K-1} \text{P}(\bar{S}_-(f_k) \leq \bar{S}(f_k) \leq \bar{S}_+(f_k)) \quad (\text{A3})$$

We reject the null hypothesis if a single estimate $\bar{S}(f_k)$ resides outside the confidence interval.

The confidence intervals $[\bar{S}_-(f_k), \bar{S}_+(f_k)]$ can be derived from the statistics of the PSD estimates $\bar{S}(f_k)$. It is easy to show that $\bar{S}(f_k)$ has an expectation value of

$$\text{E}\{\bar{S}(f_k)\} = \frac{(|\tilde{w}|^2 * S)(f_k)}{L} \quad (\text{A4})$$

Moreover, it has been demonstrated in [34] that $\frac{\nu \bar{S}(f_k)}{\text{E}\{\bar{S}(f_k)\}}$ is χ_ν^2 distributed with $\nu = 2M$ degrees of freedom. By attributing ‘‘equal confidence’’ to each of the K frequency bins we can write

$$\text{P}(\bar{S}_-(f_k) \leq \bar{S}(f_k) \leq \bar{S}_+(f_k)) = \gamma^{\frac{1}{K}} = 1 - \alpha \quad (\text{A5})$$

where α is the probability that the estimate resides outside the confidence interval. The limits $\bar{S}_-(f_k)$ and $\bar{S}_+(f_k)$ are constructed symmetrically such that

$$\text{P}(\bar{S}(f_k) < \bar{S}_-(f_k)) = \text{P}(\bar{S}(f_k) > \bar{S}_+(f_k)) = \frac{\alpha}{2} \quad (\text{A6})$$

They can be calculated by using the χ_ν^2 distributional property.

ACKNOWLEDGMENTS

The authors thank Gerhard Heinzel for the fruitful exchanges. The authors also thank the Performance Working/Expert Group and the Simulation Working/Expert Group of the LISA Consortium. This work is supported by the Centre National d’Études Spatiales (CNES), the Centre National de la Recherche Scientifique (CNRS), the Université Paris Cité (former Université Paris Diderot), the Institut de la Recherche sur les lois Fondamentales de l’Univers of the Commissariat à l’Énergie Atomique et aux énergies alternatives (CEA/IRFU) and the Observatoire de Paris. It was also supported by the Programme National GRAM of CNRS/INSU with INP and IN2P3 co-funded by CNES.

[1] P. Amaro-Seoane, H. Audley, S. Babak, J. Baker, E. Barausse, P. Bender, E. Berti, P. Binetruy, M. Born, D. Bor-toluzzi, J. Camp, C. Caprini, V. Cardoso, M. Colpi, J. Conklin, N. Cornish, C. Cutler, K. Danzmann,

R. Dolesi, L. Ferraioli, V. Ferroni, E. Fitzsimons, J. Gair, L. Gesa Bote, D. Giardini, F. Gibert, C. Grimani, H. Halloin, G. Heinzel, T. Hertog, M. Hewitson, K. Holley-Bockelmann, D. Hollington, M. Hueller, H. Inchauspe,

- P. Jetzer, N. Karnesis, C. Killow, A. Klein, B. Klipstein, N. Korsakova, S. L. Larson, J. Livas, I. Lloro, N. Man, D. Mance, J. Martino, I. Mateos, K. McKenzie, S. T. McWilliams, C. Miller, G. Mueller, G. Nardini, G. Nelemans, M. Nofrarias, A. Petiteau, P. Pivato, E. Plagnol, E. Porter, J. Reiche, D. Robertson, N. Robertson, E. Rossi, G. Russano, B. Schutz, A. Sesana, D. Shoemaker, J. Slutsky, C. F. Sopuerta, T. Sumner, N. Tamanini, I. Thorpe, M. Troebs, M. Vallisneri, A. Vecchio, D. Vetrugno, S. Vitale, M. Volonteri, G. Wanner, H. Ward, P. Wass, W. Weber, J. Ziemer, and P. Zweifel, arXiv e-prints, arXiv:1702.00786 (2017), arXiv:1702.00786 [astro-ph.IM].
- [2] LISA Science Study Team, *LISA Science Requirements Document*, Requirement Document No. ESA-L3-EST-SCI-RS-001-i1.0 (ESA, 2018) <https://www.cosmos.esa.int/documents/678316/1700384/SciRD.pdf>.
- [3] F. B. Estabrook, M. Tinto, and J. W. Armstrong, Phys. Rev. D **62**, 042002 (2000).
- [4] K. R. Nayak, S. Koshti, S. V. Dhurandhar, and J.-Y. Vinet, (2005), arXiv:gr-qc/0507105 [gr-qc].
- [5] M. Vallisneri, Phys. Rev. D **72**, 042003 (2005), [Erratum: Phys.Rev.D 76, 109903 (2007)], arXiv:gr-qc/0504145.
- [6] A. Petiteau, *De la simulation de LISA a l'analyse des donnees. Détection d'ondes gravitationnelles par interférométrie spatiale (LISA : Laser Interferometer Space Antenna)*, Theses, Université Paris-Diderot - Paris VII (2008).
- [7] M. Otto, *Time-delay interferometry simulations for the Laser Interferometer Space Antenna*, Ph.D. thesis, Leibniz Universität Hannover (2016).
- [8] J.-B. Bayle, *Simulation and Data Analysis for LISA (instrumental modeling, time-delay interferometry, noise-reduction performance study, and discrimination of transient gravitational signals)*, Theses, Université de Paris ; Université Paris Diderot ; Laboratoire Astroparticules et Cosmologie (2019).
- [9] M. Muratore, *Time delay interferometry for LISA science and instrument characterization*, Ph.D. thesis, University of Trento (2021).
- [10] O. Hartwig, *Instrumental modelling and noise reduction algorithms for the Laser Interferometer Space Antenna*, Ph.D. thesis, Leibniz Universität Hannover (2021).
- [11] O. Hartwig and J.-B. Bayle, Phys. Rev. D **103**, 123027 (2021), arXiv:2005.02430 [astro-ph.IM].
- [12] J.-B. Bayle, M. Lilley, A. Petiteau, and H. Halloin, Phys. Rev. D **99**, 084023 (2019), arXiv:1811.01575 [astro-ph.IM].
- [13] J.-B. Bayle, O. Hartwig, and M. Staab, Phys. Rev. D **104**, 023006 (2021), arXiv:2103.06976 [gr-qc].
- [14] S. Paczkowski, R. Giusteri, M. Hewitson, N. Karnesis, E. D. Fitzsimons, G. Wanner, and G. Heinzl, Phys. Rev. D **106**, 042005 (2022).
- [15] O. Hartwig, J.-B. Bayle, M. Staab, A. Hees, M. Lilley, and P. Wolf, Phys. Rev. D **105**, 122008 (2022), arXiv:2202.01124 [gr-qc].
- [16] A. Krolak, M. Tinto, and M. Vallisneri, Phys. Rev. D **70**, 022003 (2004), [Erratum: Phys.Rev.D 76, 069901 (2007)], arXiv:gr-qc/0401108.
- [17] M. Tinto, D. A. Shaddock, J. Sylvestre, and J. W. Armstrong, Phys. Rev. D **67**, 122003 (2003), arXiv:gr-qc/0303013.
- [18] J. T. Valliyakalayil, A. J. H. Sutton, R. E. Spero, D. A. Shaddock, and K. McKenzie, Phys. Rev. D **105**, 062005 (2022), arXiv:2110.10870 [gr-qc].
- [19] J.-B. Bayle and O. Hartwig, Phys. Rev. D **107**, 083019 (2023), arXiv:2212.05351 [gr-qc].
- [20] J. Sylvestre and M. Tinto, Phys. Rev. D **68**, 102002 (2003), arXiv:gr-qc/0308085.
- [21] T. Robson, N. J. Cornish, and C. Liu, Class. Quant. Grav. **36**, 105011 (2019), arXiv:1803.01944 [astro-ph.HE].
- [22] S. L. Larson, W. A. Hiscock, and R. W. Hellings, Phys. Rev. D **62**, 062001 (2000), arXiv:gr-qc/9909080.
- [23] G. Heinzl, *LISA Frequency Planning*, Technical Note No. LISA-AEI-INST-TN-002 (AEI, 2018).
- [24] Gehler, Martin *et al.* (ESA Study team), *Mission Requirement Document*, Requirement Document No. ESA-L3-EST-MIS-RS-001-i1.10 (ESA, 2021).
- [25] A. Petiteau, G. Auger, H. Halloin, O. Jeannin, S. Pireaux, E. Plagnol, T. Regimbau, and J. Y. Vinet, AIP Conf. Proc. **873**, 633 (2006).
- [26] M. Tinto and S. V. Dhurandhar, Living Rev. Relativity **17**, 6 (2014).
- [27] M. Muratore, D. Vetrugno, S. Vitale, and O. Hartwig, Phys. Rev. D **105**, 023009 (2022), arXiv:2108.02738 [gr-qc].
- [28] J.-B. Bayle, “Power spectral density python tool,” <https://pypi.org/project/psd/>.
- [29] J.-B. Bayle, O. Hartwig, A. Petiteau, and M. Lilley, “Lisanode,” (2022).
- [30] T. A. Prince, M. Tinto, S. L. Larson, and J. W. Armstrong, Phys. Rev. D **66**, 122002 (2002), arXiv:gr-qc/0209039 [gr-qc].
- [31] S. Babak, A. Petiteau, and M. Hewitson, (2021), arXiv:2108.01167 [astro-ph.IM].
- [32] M. Muratore, O. Hartwig, D. Vetrugno, S. Vitale, and W. J. Weber, (2022), arXiv:2207.02138 [gr-qc].
- [33] M. R. Adams and N. J. Cornish, Phys. Rev. D **82**, 022002 (2010), arXiv:1002.1291 [gr-qc].
- [34] G. M. Jenkins and D. G. Watts, *Spectral Analysis and Its Applications*, Holden-Day Series in Time Series Analysis (Holden-Day, San Francisco, 1968).